PNAS RESEARCH ARTICLE | CHEMISTRY

Capillary-driven self-assembly of soft ellipsoidal microgels at the air–water interface

Nabanita Hazra[a], Andrey A. Rudov[b,c], Jiarul Midya[d], Andrey Babenyshev[a], Steffen Bochenek[a], Martin Frenken[a], Walter Richtering[a], Gerhard Gompper[d], Thorsten Auth[d], Igor I. Potemkin[b,c,1], and Jérôme J. Crassous[a,1]

Affiliations are included on p. 11.

Edited by David Weitz, Harvard University, Cambridge, MA; received March 1, 2024; accepted October 27, 2024

The adsorption of ellipsoidal colloidal particles on liquid interfaces induces interfacial deformation, resulting in anisotropic interface-mediated interactions and the formation of superstructures. Soft prolate-shaped microgels at the air–water interface offer an ideal model for studying spontaneous capillary-driven self-assembly due to their tunable aspect ratio, controlled functionality, and softness. These microgels consist of a polystyrene core surrounded by a cross-linked, fluorescently labeled poly(*N*-isopropylmethylacrylamide) shell. By uniaxially stretching the particles embedded in polyvinyl alcohol films, the aspect ratio ρ can be finely adjusted. ρ was found to vary from 1 to 8.8 as estimated in their swollen conformation at 20 °C from confocal laser scanning microscopy. The spontaneous interfacial self-assembly at the air–water interface is investigated through fluorescence microscopy, theoretical calculations, and computer simulations. A structural transition occurs from a seemingly random assembly for small aspect ratios to compact clusters, which transform into a side-to-side assembly forming long chains for high aspect ratios. The influence of the poly(*N*-isopropylmethacrylamide) shell on the assembly indicates a significant ρ-dependent microgel deformation. This deformation, in turn, determines the average distance between the particles. Consequently, capillary-driven self-assembly of soft anisotropic colloids becomes a powerful mechanism for structuring interfaces and designing microstructured materials.

microgels | anisotropic colloids | fluid interfaces | self-assembly | capillary interactions

Thermoresponsive poly(*N*-isopropylacrylamide) (PNIPAM) or poly(*N*-isopropylmeth acrylamide) (PNIPMAM) microgels are fascinating systems at the crossover between colloids, polymers, and surfactants (1–3). Their ambiguous nature stems from their fuzzy structure, which allows them to interpenetrate, facet, and/or deswell in crowded environments (4, 5). Temperature not only affects their size but also facilitates precise control of interparticle interactions, influencing their assembly behavior (6). Brought at fluid interfaces, in analogy to surfactants, microgels are surface active and were found to efficiently stabilize interfaces, which has motivated their use as smart stabilizing agents for emulsions (7, 8). Hereby, their responsivity to temperature can be employed to control the stability of the emulsion. The latter properties stem from their polymer/colloid duality and ability to deform strongly and spread at the interface (9). Again, their size, cross-linking, and structure (homogeneous, core-shell, and hollow) are key determinants when examining their organization at the interfaces (10). Despite the significant number of studies dealing with their interfacial properties, many questions remain unanswered regarding the nature of their interactions at the interface.

Capillary interactions for hard colloids at interfaces arise from the deformation of the surrounding interface induced by the particles (11–13). To minimize the total interfacial energy, particles tend to self-assemble in configurations that maximize the overlap of induced interfacial deformations. A planar interface may be distorted by the surface roughness of the colloids (14), gravity and flotation forces (15), and a nonspherical colloid shape (16, 17). A very rich assembly behavior at fluid interfaces is found for cylindrical and cube-like colloids (18, 19), for colloids at curved interfaces (20, 21), or if in addition to interface deformation, direct interactions are involved, such as electrostatic repulsion (22, 23). For ellipsoids, it has been shown analytically and experimentally that the interfacial deformation is at the origin of quadrupolar interactions between the colloids. (24, 25). Here, the contact angle that satisfies the Young–Laplace equation can only be achieved all around the particle if the contact line's height and interface surrounding the particle are deformed. Assemblies driven by the long-ranged capillary

Significance

Capillary interactions arise when colloids adsorb at and distort fluid interfaces. This effect is particularly relevant for anisotropic colloids pinned at fluid interfaces due to the nonconstant curvature of their surfaces. When the colloids are themselves strongly deformable, there is an interesting interplay of interface and particle deformation. To study this effect, model ellipsoidal core-shell microgels, consisting of a stiff core surrounded by a crosslinked swollen polymeric network, were obtained via uniaxial elongation of the original spherical systems. Their interfacial assembly at the air–water interface demonstrates that i) these systems significantly spread laterally and that ii) capillary interactions either favor side-by-side or tip-to-tip assembly, which drives the assembly from compact triangular to side-by-side linear aggregates with increasing aspect ratio.

Author contributions: N.H., I.I.P., and J.J.C. designed research; N.H., A.A.R., J.M., A.B., S.B., M.F., G.G., T.A., I.I.P., and J.J.C. performed research; N.H., A.A.R., J.M., A.B., S.B., M.F., T.A., I.I.P., and J.J.C. analyzed data; and N.H., A.A.R., J.M., A.B., W.R., G.G., T.A., I.I.P., and J.J.C. wrote the paper.

The authors declare no competing interest.

This article is a PNAS Direct Submission.

[1]To whom correspondence may be addressed. Email: potemkin@dwi.rwth-aachen.de or crassous@pc.rwth-aachen.de.

This article contains supporting information online at https://www.pnas.org/lookup/suppl/doi:10.1073/pnas.2403690121/-/DCSupplemental.

Published December 20, 2024.

attraction have been explored both experimentally and theoretically. Capillary chain-like assemblies with colloids arranged in tip-to-tip and side-by-side orientations, as well as flower-like assemblies and triangular network structures, have been reported for ellipsoids depending on their aspect ratio and the contact angle value (16, 22). The interactions are usually of the order of tens/hundreds of k_BT. Therefore, although the assembly may change on the time scale of hours (22), not only the minimal energy conformation but also the kinetics of the structure formation determine the structures that are observed; for example, for three particle aggregates, linear side-by-side and triangular assemblies are often simultaneously encountered in experiments (26). In addition, it was shown through phase shifting interferometry (PSI) measurements, in the case of polystyrene ellipsoids obtained via uniaxial elongation (27), that the stretching process may significantly affect the contact angle through the delocalization of the functional groups present at their surface of the particles (24).

However, one might inquire what is happening for soft/deformable systems such as microgels, which are strongly flattened at the interfaces (28–31). Even if interfacial examination using, for instance, Fresca provides clear evidence of the protrusion of such microgels at the interface, the usually observed fried-egg microgel configuration at the interface makes it challenging to define any contact angle (31, 32). Surprisingly, "small" microgels, at least in comparison to hard colloids, exhibiting flotation forces with a swollen hydrodynamic radius typically larger than circa 300 nm were also found to display capillary interactions. The effect seems to be enhanced in the case of core-shell microgels, as their cores restrict their interfacial spreading and positioning. Given the negligible buoyancy of these swollen particles, the underlying mechanism driving this phenomenon is likely attributed to elastocapillary interactions. However, we are still far from fully understanding the interfacial assembly of microgel-based systems. In this field, a central question is the interfacial assembly behavior of microgels under compression and the onset, in many cases, of an isostructural transition from one crystalline organization to another one. Again, capillary interactions may play an important role, particularly at high compressions where the topology of the interface is altered, even if it has not been clearly established yet. The situation becomes more complex when dealing with anisotropic microgels (16). Silica-coated hematite/PNIPAM core-shell microgels are striking examples. The interfacial assembly behavior was found to strongly depend on the anisotropy of the particles and the cross-linking/swelling of the microgel shell (33, 34). Hereby, harder and more anisotropic microgels spontaneously exhibited strong capillary interactions. In contrast, softer microgels with a comparable mass were only assembled via capillary interactions at more significant compressions. Further on, core-shell ellipsoidal microgels synthesized via seed polymerization using stretched polystyrene core as seeds were found to display strong capillary interactions and to form robust string-like capillary assembly as the consequence of the interpenetration of their microgel shells (35).

In this study, we explore the influence of both anisotropy and softness on the capillary assembly of prolate-shaped core-shell microgels. Initially, spherical core-shell microgels were post-processed into prolates through uniaxial stretching, as detailed in our former study (36, 37). We examined the spontaneous capillary assembly of the microgels at the air–water interface as a function of the aspect ratio of the particles. As shown from our calculation, a clear transition from a disordered assembly to a side-by-side configuration going through an intermediate, mostly triangular assembly was observed, as expected for hard prolate particles. Interestingly, conversely to hard particles, the microgels-based anisotropic microgels were found to spread at the interface resulting in a larger spacing between the particles. We extracted the extent of the particle deformation at the interface along the long and short axes of the prolates from the different conformations. The experimental results were then compared to computer simulations using coarse-grained core-shell microgels deformed in cylindrical confinement to reproduce the uniaxial stretching process at different draw ratios. The particle deformation at the interface and the air–water interface deformation are further discussed concerning the anisotropy of the core-shell microgels and the local structure of the microgel shell based on the experimental and simulation results.

Anisotropic Core-Shell Microgel Characterization

The core-shell microgels have already been characterized in a former study by Transmission Electron Microscopy (TEM) and Confocal Laser Scanning Microscopy (CLSM) (37). We refer to this study for further details on the measurements. The different particles and their conformation in dispersion are illustrated by representative TEM and CLSM micrographs in Fig. 1 (37). These two techniques provide essential information on the conformation of the different systems. Indeed, TEM micrographs characterize the system in the dried state, for which the microgel shell is completely collapsed, whereas CLSM micrographs were recorded in the swollen state on microgels adsorbed at the glass slide. It allows for better determination of the dimensions, as all the microgels are almost in the same imaging plane. Hereby, we benefit from the system being highly monodisperse and presenting a clear core-shell structure. The focus can therefore be easily set on the midsection of particles laying "flat" at the interface. The dimensions of the different core-shell microgels determined by these two techniques, obtained from the statistical analysis of more than 100 particles, are summarized in *SI Appendix*, Table S1. Note that an evaluation of the dimensions in bulk is far more challenging (and inaccurate) due to the fast diffusion of the systems. Only microgels laying "flat" have been considered for the analysis.

The spherical core-shell microgels shown in Fig. 1 have an overall diameter of 623 ± 31 nm and a core diameter of 534 ± 50 nm determined from TEM analysis. Highly monodisperse microgels with core-shell structures are visible from the CLSM micrograph. The CLSM micrograph in Fig. 1 was taken from a concentrated dispersion where the particles were assembled into hexagonal crystals, confirming the starting materials' quality before processing. After transformation, the different core-shell ellipsoidal microgels appear highly defined, with respect to their ellipsoidal shape, and uniform, accounting for their size and anisotropy. This was confirmed from the statistical analysis to determine their long and short full axes $2a$, $2b$, and aspect ratio $\rho = a/b$ as a function of the film draw ratio λ. The analysis of the TEM and CLSM micrographs recorded for $\lambda = 1.50$ to 2.00, confirms that the particles present low polydispersity in terms of size and shape in the order of 6 to 7% for $2a$, $2b$, and ρ. At the highest draw ratio ($\lambda = 5.00$), the particles were found to deviate slightly from the ellipsoidal shape. They present some tortuosities, primarily visible from the TEM imaging, in contrast to the case of pure polystyrene latex, where it does not occur (27, 38). Keeping in mind that the PNIPMAM shell is cross-linked, we may expect considerable constraints to develop within

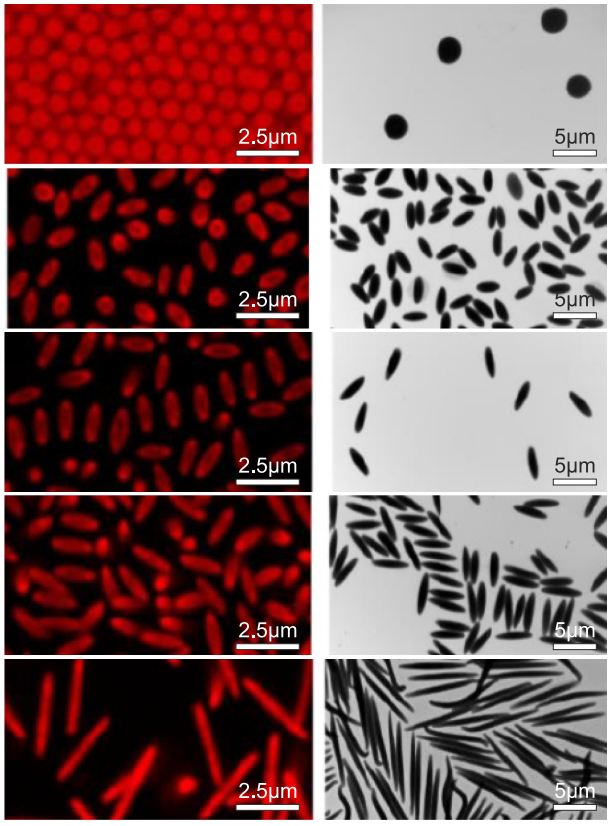

Fig. 1. Representative CLSM (*Left*) and TEM (*Right*) micrographs of the different prolate-shaped soft microgels obtained for different draw ratio λ. From *Top* to *Bottom*: original $\lambda = 1.00$, 1.50, 1.75, 2.00, and 5.00 (Reproduced from ref. 37).

the materials at high elongations, mainly concentrating on the tips. Thus, the conformation of the microgel shell is highly likely to be affected by the stretching procedure. Consequently, they do exhibit a higher polydispersity, which is in the order of 14 and 8% for ρ from TEM and CLSM imaging, respectively. Considering that the particles are core-shell with a soft microgels shell, we note that the aspect ratio determined by TEM is significantly larger than by CLSM as indicated in *SI Appendix*, Table S1. Therefore, we expect that the aspect ratio of the system can be altered with the temperature.

The proper dispersion of the different systems was confirmed by CLSM measurements, as shown in the former study discussing their dipolar self-assembly under an alternating electric field (37). We also confirmed this point by checking the quality of the dispersions using either bright field or fluorescence microscopy. We then proceeded with the characterization of the different particle swelling behavior by Dynamic Light Scattering (DLS) (*SI Appendix*, Fig. S1) (39). The original spherical core-shell microgels were first compared to redispersed core-shell particles that were embedded in a PVA (polyvinyl alcohol) film and exposed to a similar thermal treatment as the ellipsoidal microgels. The swelling behavior of both systems is almost identical, confirming the absence of residual PVA and that the thermal history of the sample does not affect its thermoresponsive properties. The analysis of the translational diffusion coefficient D_T of the ellipsoidal microgels further illustrates the influence of the microgel anisotropy and stretching procedure on the diffusion of the particle. We refer to *SI Appendix* for further details on this analysis.

Capillary Assembly of Hard Ellipsoids

For hard ellipsoids pinned at a fluid interface, with their long axis parallel to the interface, the contact line with the liquid is defined by the contact angle α and the local particle-surface curvature. The contact line is higher along the short axis (high curvature) and lower along the long axis (low curvature) (16, 24). The corresponding interface distortion is responsible for capillary interactions that tend to minimize the total surface energy by assembling the particles. In order to obtain qualitative understanding, we considered an approximate analytic description of the contact line accounting for the local curvature of a wetted ellipsoid lying parallel to the interface (see *SI Appendix*, Fig. S2 and details for the calculation in *SI Appendix*) (39). The height difference of the contact line between the short and long axes, Δz, was considered in the case of an isochoric transformation from sphere ($R_0 = 500$ nm) to prolate for different contact angles (*SI Appendix*, Fig. S2*A*). For $\alpha = 40°$, which is in the order of the reported value for PNIPAM hydrogels (40, 41), we did observe a rapid increase of Δz with ρ up to $\rho = 5$ followed by a slight decrease with increasing ρ (*SI Appendix*, Fig. S2*B*). From this simple calculation, it is therefore expected that capillary interactions become more prominent with increasing the aspect ratio of the ellipsoidal microgels at the condition they would not deform at the interface. However, such calculations do not account for the whole system and multibody effects corresponding to different assemblies.

Therefore, simulations were performed on hard ellipsoids to predict the interfacial assembly when it is solely driven by ρ and α. The minimization of the total interfacial energy then allows us to predict stability of triangular and linear assemblies of ellipsoidal hard particles; see Fig. 2*A* and *SI Appendix*, Fig. S3. Stable triangular assemblies were found at low particle aspect ratios and stable linear assemblies at high particle aspect ratios. For three-particle systems, the stability of the triangular assembly shifts to higher aspect ratios with increasing contact angles. The aspect ratio for the transition monotonically increases from $\rho^*(\alpha = 30°) \approx 1.5$ to $\rho^*(\alpha = 85°) \approx 6$. Comparing the energies per particle for a hexagonal bulk phase and an infinitely long linear chain, linear chains are stable for either high aspect ratios or small contact angles. The hexagonal phase is stable only for particles with small aspect ratios and contact angles. The transition occurs at $\rho^*(\alpha = 85°) \approx 2$ and the hexagonal phase vanishes entirely for contact angles $\alpha \leq 40°$. For the systems with typical structures formed by more than three particles but not as ordered as homogeneous bulk phases, we expect the transition to occur in between these two phase boundaries for the three-particle and the bulk system.

Fig. 2 *B*–*E* and *SI Appendix*, Fig. S4 show interface deformations around linear and triangular particle aggregates. The interface is pulled up at the sides and pushed down at the tips of single ellipsoidal particles. Overlap of alike interface deformations decreases the total interface area and, consequently, provokes particle–particle attraction and aggregation. Increasing the ellipsoid aspect ratio increases both, the height deformation along the contact line where the interface detaches from the particle and the length for that the contact line is raised along the sides of the particles. Therefore, increasing the particle aspect ratio favors side-by-side aggregation. However, the interface deformation around the entire aggregate is much smaller for triangular aggregates than linear aggregates, suppressing linear aggregates for three-particle systems. For bulk systems (aggregates with many particles), the deformation energy of the interface surrounding the aggregates can be neglected. Thus, for many-

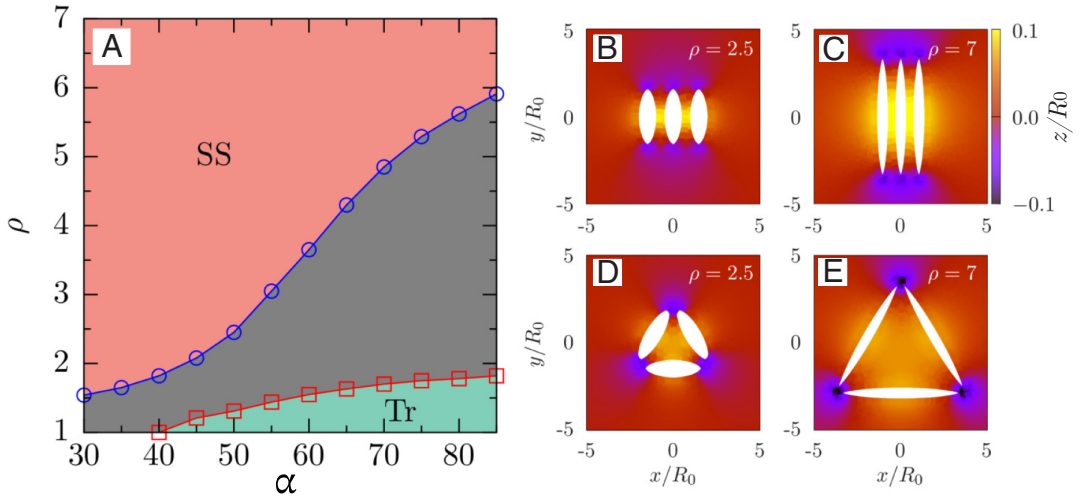

Fig. 2. Structures and interface deformations for aggregates of ellipsoidal hard particles at interfaces. All particles have the same volume as a sphere with a radius R_0. (*A*) Phase diagram for various contact angles α and particle aspect ratios ρ. Blue circles indicate the phase boundary between side-by-side (*SS*) and triangular (*Tr*) three-particle aggregates, and red squares the phase boundary between a linear aggregate and a hexagonal bulk phase. In the gray-shaded area, triangular three-particle aggregates and linear infinitely long chains are stable. (*B–E*) Interface deformations around linear and triangular three-particle aggregates for $\alpha = 60°$ and particle aspect ratios (*B* and *D*) $\rho = 2.5$ and (*C* and *E*) $\rho = 7$. The interface height along distinguished cuts that correspond to high symmetries is shown in *SI Appendix*, Fig. S4.

particle systems, linear aggregates are stable in a larger parameter regime.

Capillary Assembly of Ellipsoidal Microgels

We now turn our attention to the spontaneous interfacial assembly of these ellipsoidal microgels at the air–water interface. To resolve the capillary assembly at the single particle level, a magnetically closed cell design is employed where a thin dispersion film with a microgel concentration of 0.01 wt% is sealed within a narrow chamber (we refer to *SI Appendix*, Fig. S5 for further detail on the cell design). The thin film thickness, which varies in the center of the cell between 70 to 80 μm depending on the sample preparation, allows visualizing the particles directly at the interface. The sealed cell design further allows for examining the sample for more than 24 h.

The spherical core-shell microgels were found to adsorb at the interface but mainly were present as single particles and did only sparsely associate into small clusters with an apparent hexagonal symmetry. The spherical soft microgels do not appear to present strong capillary interactions, whereas ellipsoidal particles assemble into large structures at the interface. This already happens after the first ten minutes. The results of the interfacial assembly for the different soft microgels are presented in Fig. 3, where the micrographs are recorded after 24 h (39).

Similar to the simulations of hard ellipsoids, a transition from triangular to side-to-side is observed with an increasing draw ratio. Indeed, the less anisotropic ellipsoidal microgels ($\lambda = 1.5$) shown in Fig. 3*A* assemble mostly into dense clusters with only a few free particles or small clusters. The assembly appears relatively disordered at first sight, as none of the tip-to-tip, side-to-side, or triangular configurations seems to prevail. Conversely, highly anisotropic particles with $\lambda = 5.00$, shown in Fig. 3*D*, almost exclusively assemble into side-to-side chains except for the junctions between particular chains, which present a well-defined, almost equilateral triangular conformation. The

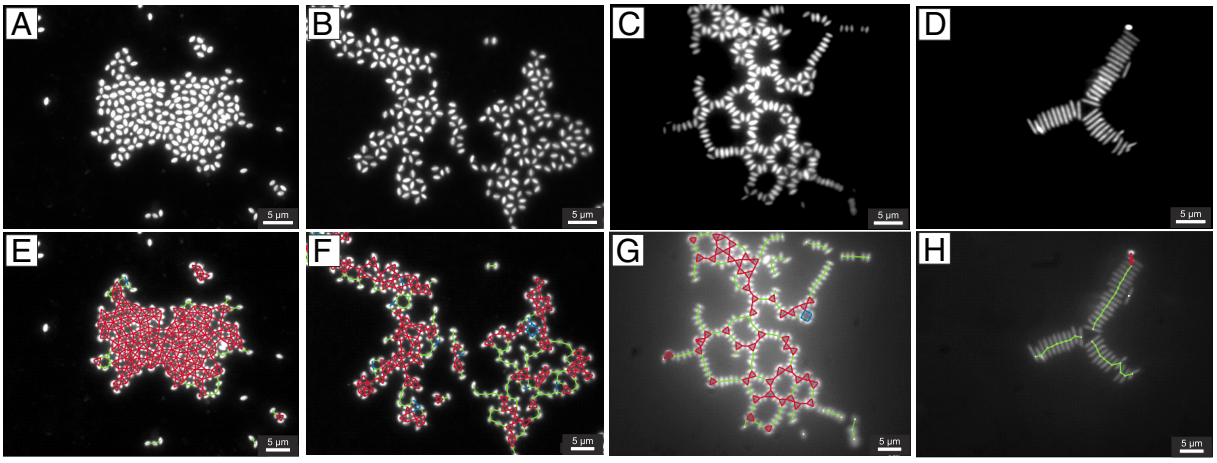

Fig. 3. (*Top*) Typical micrographs of the capillary-driven interfacial assembly recorded at the air–water interface after 24 h for soft ellipsoidal microgels with different draw ratios under dilute conditions (0.01 wt% dispersion). From *Left* to *Right* λ = 1.50 (*A*), 1.75 (*B*), 2.00 (*C*), and 5.00 (*D*). (*Bottom*) Analysis by Delaunay triangularization evidencing the triangular (red), square (blue), tip-to-tip and side-to-side (green) organization of the particles at the interface for λ = 1.50 (*E*), 1.75 (*F*), 2.00 (*G*), and 5.00 (*H*). With increasing λ, a transition from compact disorder to elongated side-to-side assembly is observed. (Scale bars: 5 μm.)

transition between these two states was detected for the intermediate draw ratios $\lambda = 1.75$ and 2.00 (Fig. 3 *B* and *C*). For $\lambda = 1.75$, the triangular assembly appears much more prominent, with little occurrence of the side-to-side assembly (Fig. 3*B*). In comparison, $\lambda = 3.3$ exhibits clear side-to-side self-assembly with very clear equilateral triangular junctions (Fig. 3*C*).

The transition from triangular to side-to-side self-assembly was quantified from image analysis. The Delaunay triangulation shown in Fig. 3 *E*–*H* distinguish between particles presenting a triangular (red) and square (blue) assembly and the one associated side-to-side and tip-to-tip (green). The transition from a triangular to side-to-side is visible with increasing λ. The particle distribution of about 20 typical micrographs for the spherical system and more than 60 for each different anisotropic microgel was statistically quantified. Before coming to the details of the analysis, we will define some of the assembly configurations that the particles may adopt at the interface.

In the following, we assume that the soft microgels maintain their ellipsoidal shape at the interface, which seems justified when looking at their shape at the interface. The different configurations that we have considered are summarized in *SI Appendix*, Fig. S6. For this analysis, we consider that the organization of the particles is set by their configuration at the interface and that the different configurations are defined as ellipses in close contact. From geometrical considerations, we can determine the center-to-center distances corresponding to the different self-assemblies, as discussed in detail in *SI Appendix*. For a defined aspect ratio, a single configuration satisfies each assembly. Ideally, only one set of parameters defining the ellipsoidal contact area, a_{int} and b_{int} should describe the side-to-side, *SS*, tip-to-tip, *TT*, triangular, *Tr*, square *Sq* and flower-like *Fl* configurations. The center of mass of each particle in the focal plane was first determined from the Matlab routine described in *SI Appendix, Experimental*. The average center-to-center distance of the particles present in "ideal" configurations was evaluated to derive the corresponding short and long axes of the microgels at the interface as shown in *SI Appendix*, Fig. S7 *A–D*.

The average 2*D* pair correlation functions, $2D\ g(r)s$, was then computed from all the configurations that are summarized for the five different draw ratio ($\lambda = 1.00$, 1.50, 1.75, 2.00, and 5.00) in Fig. 4*A* (39). For the sphere ($\lambda = 1.00$), the average $2D\ g(r)$ shows very few features, considering that most single particles are adsorbed at the interface. From the few clusters present, we can detect the nearest neighbor distance, which we define as d_{SS}. Additionally, a few clusters with a hexagonal symmetry were recorded, corresponding to the two weak extra peaks that could be defined as a function of $d_{SS} = 870$ nm following a 2*D* hexagonal lattice as $\sqrt{3}d_{SS}$ and $2d_{SS}$, respectively. It turns out that the diameter determined from the analysis was very close to the diameter determined by CLSM, as illustrated in Fig. 4*B*. This value is about 100 nm lower than the hydrodynamic diameter, $2R_H = 972$ nm determined at the same temperature pointing to the compression and/or interpenetration of the microgels involved in the capillary assembly. The $2D\ g(r)$ derived for λ

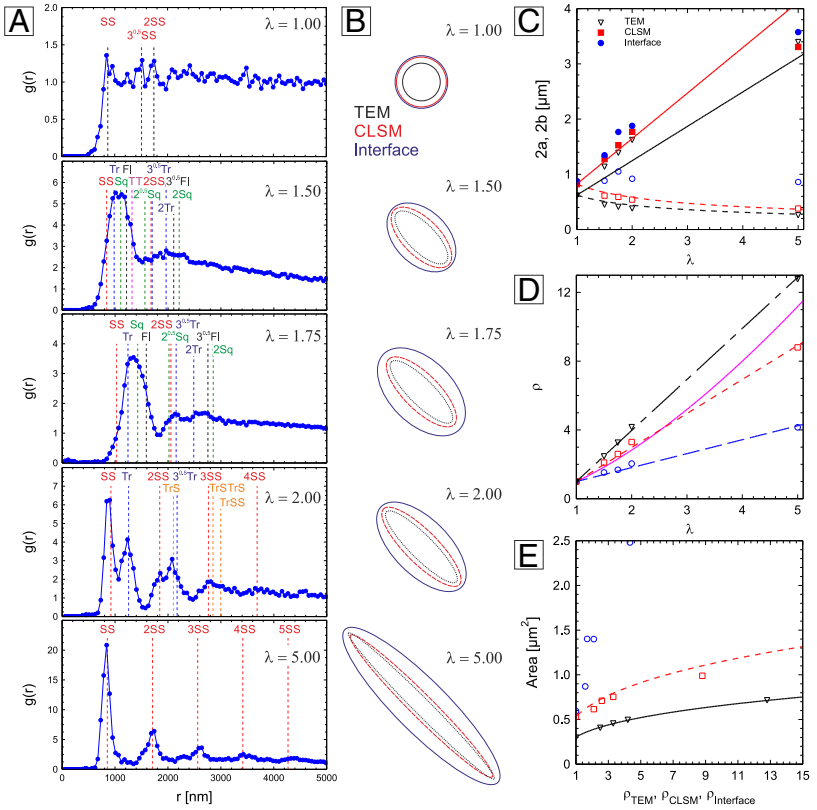

Fig. 4. (*A*) 2D pair correlation functions of the core-shell microgels obtained for the different draw ratios. The short and long-axis dimensions at the interface are estimated from the 2*D* characteristic assemblies of ellipsoids at contact indicated by dotted lines. (*B*) Schematic representations of the overall dimensions of the core-shell microgels drawn to scale as determined from their configuration in their collapsed state (TEM, dotted lines), swollen state (CLSM, dashed lines), and at the air–water interface (from the analysis of their self-assembly at contact assuming an ellipsoidal shape, solid lines). Evolution of the full short and long axes (*C*) and aspect ratio (*D*) determined by TEM, CLSM, and from the interfacial assembly plotted as a function of the draw ratio. The solid and dotted lines in (*C*), are the predictions for cold stretching. The dashed, dotted, and dash-dotted lines in (*D*) illustrate the linear dependence of ρ on λ. The solid line corresponds to the prediction for cold stretching. (*E*) Projected surface areas are determined by TEM and CLSM. The interfacial area is derived from the capillary assembly as a function of the corresponding aspect ratio. Solid and dashed lines show the expected evolution of the projected area under an isochore deformation.

$= 1.50$ is characterized by a surprisingly high and broad first peak followed by a wider shoulder. The broadness of the peak is related to the absence of clear preferential assembly.

The distances corresponding to the different configurations from the former analysis are added to the graph. We can notice here that many configurations have close characteristic distances that are all included in the first peak, with increasing distances *SS*, *Tr*, *Sq*, and *Fl*. At a higher draw ratio of $\lambda = 1.75$, the first peak presents a lower height but is still significant and broad. The following shoulder becomes more structured and presents an additional splitting as the assembly becomes more defined. From the analysis of the characteristic distances, we observe that the *Tr* and *Sq* appear to dominate with a preference for *Tr* that is visible from the second and third peak higher-order maxima. The transition from triangular to side-to-side occurs between $\lambda =$ 1.75 and 2.00. For $\lambda = 2.00$, both the *SS* and *Tr* configurations are identified and very well-defined, as revealed by the sharp peaks in the 2*D* $g(r)$. Finally, for $\lambda = 5.00$, the assembly is essentially *SS*, including higher-order peaks corresponding to the periodicity of the *SS*-stacking. The first peak is extremely sharp, indicating that the particles position themselves almost always at the same distance.

Particle Deformation at the Interface

Looking back into the assembly of the stretched core-shell microgels with $\lambda = 2.00$, which shows clear side-by-side self-assembly, we can notice that the nearest neighbor distance corresponding to side-by-side self-assembly is much larger than the dimensions determined via CLSM. Unlike their spherical counterparts, the ellipsoidal microgels are flattened and spread at the interface. This is also directly visible on the fluorescence micrographs from a closer examination of some of the particles at the interface in Fig. 3 and the presence of a diffuse corona at the sides of the ellipsoids.

The particle deformation at the interface of the different ellipsoidal microgels is schematically summarized in Fig. 4*B* in comparison to the dimensions determined from CLSM and TEM analysis. Interestingly, we can observe that the particles appear to spread more laterally than longitudinally. In fact, the long axis seems to exhibit tiny variations between its dried and swollen states and at the interface.

We further summarized the different analyses. The evolution of the full long and short axes is displayed in Fig. 4*C* (39). TEM and CLSM measurements are compared to the predictions for isochoric transformation under cold stretching conditions, *i.e.*, the particles and the film experience the same deformation (36). One then expects that $2a = 2R_{\lambda=0} \times \lambda$, $2b = 2R_{\lambda=0} \times \lambda^{-\frac{1}{2}}$ and $\rho = \lambda^{\frac{3}{2}}$. The TEM dimensions indicate that the particles get significantly more deformed than the film during the elongation. When looking at the CLSM, the cold stretching scaling nicely describes their deformation. As far as the dimensions at the air–water interface are concerned, the linear scaling holds for the long axis both for the dried and swollen states. Instead of decreasing, the full short axis remains almost constant due to the lateral microgel deformation at the interface.

The evolution of the aspect ratios as a function of λ is summarized in Fig. 4*D* (39). For the three cases, ρ almost scales linearly with λ such that $\rho_{TEM} \approx 2.97 \times \lambda$, $\rho_{CLSM} \approx 1.98 \times \lambda$ and $\rho_{\text{int}} \approx 0.81 \times \lambda$. Finally, in Fig. 4*E*, we report the evolution of the projected area, *A*, as a function of the aspect ratio determined by TEM, CLSM, and at the interface. For the core-shell microgels in the dried and swollen state, *A* is comparable to the expected projected area from nondeformable ellipsoids, $A \approx \pi R^2_{\lambda=0} \times \rho^{\frac{1}{3}}$ indicating that the particles do not significantly deform either at the carbon grid or the glass. Conversely, it does not hold at all for the ellipsoidal microgels at the air–water interface, for which the contact area dramatically increases with ρ. This is again clearly visible from the fluorescence micrographs, where the particles appear much more prominent with increasing draw ratio. We further performed atomic force microscopy measurements to support the characterization of the particles and their interfacial assembly (39). This investigation reveals the different assemblies observed after transferring the particles to a solid substrate via dipcoating (*SI Appendix*, Fig. S8), as well as the local stiffness and spreading of the particles deposited on the solid substrate after rehydration (*SI Appendix*, Figs. S8 and S9 and Table S2 and Movies S1–S3). We refer to *SI Appendix* for further details on this analysis.

Based on the different experiments, we can now compare the values obtained for ρ to the hard ellipsoid phase diagram as shown in *SI Appendix*, Fig. S7*E*. Considering that the transition between the *Tr* and *SS*-configurations takes place between $\lambda = 1.75$ and 2.00, the soft ellipsoids effectively behave as hard ellipsoids with an effective contact angle in the order of 40° at the interface. The same analysis performed using the ρ-values from the CLSM and TEM analysis leads to effective contact angles of approximately 54° and 61°. When the contact angle of 40° seems in line with the reported values for PNIPAM, it is clear that the microgels are highly flattened at the interface and that the interface deformation should take place closer to the interface between the hard core and soft shell. The other two values fall between the reported contact angles of PNIPAM (40, 41) and pure polystyrene, which is in the order of 90° (42). It is noteworthy that for polystyrene ellipsoids, the latter value is strongly dependent on surface functionalization and may be affected by the uniaxial elongation process. In such cases, the reported values are much lower than those for pure polystyrene, ranging between 48° and 33° (24). Therefore, the observed assembly results from the anisotropic deformation of the particles at the interface and the interfacial deformation, which depends on the interfacial properties of the solid polystyrene core and soft microgel shell, as will now be discussed in *Coarse-Grained Modeling*.

Coarse-Grained Modeling

A coarse-grained model of anisotropic ellipsoidal soft particles was developed. We obtained a series of core-shell (PS/PNIPMAM) ellipsoidal microgels with different aspect ratios. Similarly to the experiment, we realized the uniaxial deformation of the spherical core-shell microgels. However, instead of deploying the mechanical stretching technique, we used a cylindrical pore as a confinement; see *SI Appendix*, Figs. S10–S13 (for further details, we refer to *SI Appendix*, *Experimental*.

We performed Dissipative Particle Dynamic (DPD) simulations of anisotropic ellipsoidal soft particles in bulk. We characterize the dimensions of different core-shell microgels by measuring the major and minor semiaxes and aspect ratio of both the solid cores (a_c, b_c, and $\rho_c = a_c/b_c$) and polymeric shell (a, b, and $\rho = a/b$) as a function of the pore characteristic, $\lambda_p = (R_0/R)^2$, where R is the pore size, while R_0 is the size of the spherical microgel in the bulk solution. We varied λ_p between 1 and 4.5. Linear size values are expressed in units of cutoff radius, r_c, which characterizes the size of a coarse-grained bead. To facilitate dimensionless analysis, all dimensional quantities were normalized by the size of the spherical core, $r_0 = a_c =$

b_c when λ_p=1. Thus, for example, the dimensionless major and minor semiaxes of the core are denoted as $\bar{a}_c = a_c/r_0$, $\bar{b}_c = b_c/r_0$, respectively, while those of the polymeric shell are $\bar{a} = a/r_0$ and $\bar{b} = b/r_0$.

To determine the dimensions of the microgels, two complementary methods were employed. First, the form factor of the core-shell microgel was calculated and fitted to an ellipsoidal model (43) using the SasView (ver. 5.0.4) software package (*SI Appendix*, Fig. S14). The obtained parameters were the semimajor and semiminor axes of both the core (a_c, b_c) and the microgel shell (a, b). All linear dimensions were normalized by the radius of the spherical core, $r_o = a_c = b_c = 8.3 \pm 0.2 r_c$. The results are presented in Fig. 5 (39). The average values of semimajor and semiminor axes of the solid core were observed to be between (1,1) → (3.28 ± 0.02, 0.54 ± 0.01). In this deformation range, the average core aspect ratio, ρ_c, was found to vary between 1 and 6.1 (Fig. 5*C*, gray symbols). For swollen microgels in bulk, the aspect ratio, ρ, ranged from 1 to 3.41 (Fig. 5*C*, red symbols). ($2\bar{a}$, $2\bar{b}$) were observed to be between (3.23 ± 0.01, 3.23 ± 0.01) → (7.69 ± 0.03, 2.25 ± 0.01) see Fig. 5*A*, red symbols. Upon increasing the temperature, the microgel underwent a collapse transition. The dimensions of the collapsed microgel ($2\bar{a}$, $2\bar{b}$) ranged from (2.52 ± 0.01, 2.51 ± 0.01) to (6.87 ± 0.05, 1.48 ± 0.01) (Fig. 5*A*, black symbols). In contrast to the swollen state, the collapsed microgels exhibited significantly larger aspect ratios, consistent with experimental observations (TEM vs. CLSM). The average microgel aspect ratio, ρ, for collapsed microgels, varied between 1 and 4.63 (Fig. 5*B*, black symbols). Notably, the aspect ratio for both states exhibited a linear dependence on the elongation parameter, λ_p, with $\rho_{\text{collapsed}} \approx 1.06 \times \lambda_p$ and $\rho_{\text{swollen}} \approx 0.69 \times \lambda_p$.

The second method is to assess the surface of a particle (44, 45) and approximate it by an ellipsoid using the least squares (LSQR) algorithm technique (46). The results are summarized in *SI Appendix*, Fig. S15. In that case, the normalization parameter $r_o = a_c = b_c = 8.63 \pm 0.14 r_c$, which is slightly larger than the one obtained by the first method (*SI Appendix*, Fig. S15*A*). When comparing the results obtained from the two methods, it appears that the scattering analysis yields slightly lower values of semimajor and semiminor axes with respect to the surface analysis. The scattering-based technique provides a structure-related analysis of the microgels based on the distribution of scattering centers within the gel. In contrast, the surface analysis only considers the peripheral fuzzy part of the microgels. Nevertheless, despite the slight differences in the values obtained by the different methods, we observed a linear dependence of ρ on λ_p. It indicates that spherical microgels deform affinely in the cylindrical confinement in the direction of the main axis and that the core retains its total mass and volume (*SI Appendix*, Fig. S12).

It is worth noting that we also monitored the stress response of the polymer shell during deformation. As the aspect ratio of microgel increases, load redistribution is intrinsically captured. We followed the distribution of junction points between the polymeric shell and the PS core (*SI Appendix*, Fig. S13). We observe a decrease in the local concentration of the junctions near the side of the core as compared to the tip, where, by contrast, we see an excess of junctions. It causes the polymeric network to stretch harder at the tips and shift the polymer mass closer to the sides. Thus, we confirm the presence of considerable constraints of the polymeric network within the microgels obtained at high elongations, mainly concentrated on the tips.

We further performed DPD simulations of anisotropic ellipsoidal soft particles at the air–water interface. We analyzed the structural changes of individual microgels and estimated the interface deformations. Equilibrium structures of the anisotropic core-shell microgels of different aspect ratios at the air–water interface are shown in Fig. 5. Analyzing the height profile, three regions within the microgels are distinguishable: (i) the area of the protrusion of the microgel into the air, (ii) a thin polymer layer at the interface (corona), and (iii) part of the microgel swollen in water (immersed part). The major and minor axes and aspect ratio of the microgels in the region (ii) are plotted in Fig. 5 *B* and *C*, blue symbols. The values were obtained by analysis of lateral slices of the microgels at the water/air interface (*SI Appendix*, Figs. S16 and S17). After adsorption, the microgels become significantly stretched at the interface. Despite the increase in the in-plane dimensions, the anisotropy of the microgels diminishes compared to the bulk solution. Consistent with experimental observations, the microgels spread relatively more laterally than longitudinally. For microgels with lower aspect ratios, this behavior was primarily attributed to the minimization of water–air interfacial energy. However, for highly anisotropic microgels, network constraints

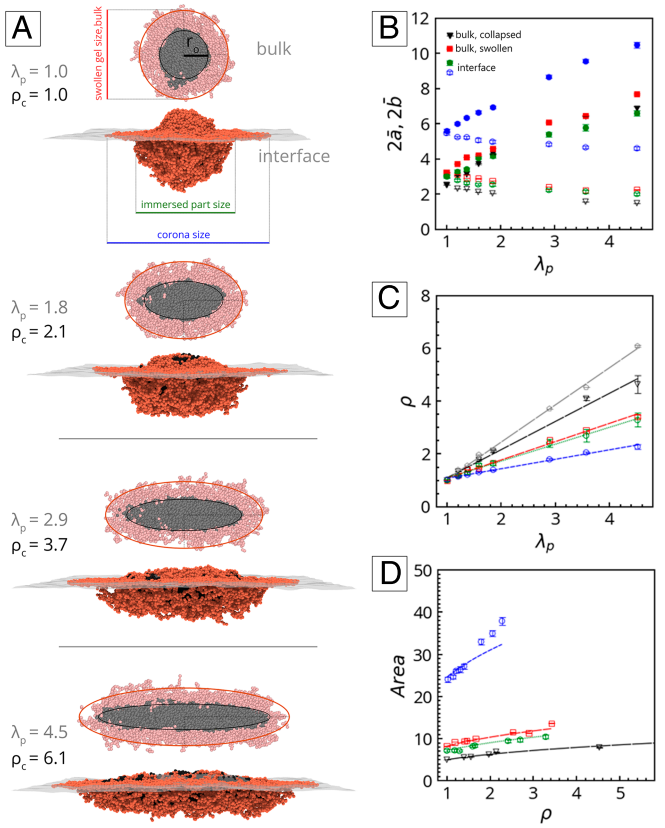

Fig. 5. Modeling of the ellipsoidal core-shell microgels obtained in the cylindrical pores of different diameters, $\lambda_p = (R_0/R)^2$. (*A*) Representations of the overall dimensions of the core-shell microgels in a swollen state (cross-sectional snapshot of the equilibrated soft microgel) and at the air–water interface (3D snapshot of the microgel) with increasing aspect ratio. Evolution of the full short and long axes (*B*) and aspect ratio (*C*) determined in bulk (black triangles and red squares correspond to the swollen and collapsed states) as well as at the air–water interface as a function of λ_p. We distinguish between the immersed microgel body (green dots) and the highly stretched PNIPMAM shell at the interface (blue dots). Gray pentagons are the dimensions of the solid core. The dashed, dotted, and dash-dotted lines in (*C*) illustrate the linear dependence of ρ on λ_p. (*D*) Projected surface areas derived as $\pi\bar{a}\bar{b}$. Solid and dashed lines show the expected evolution of the projected area under an isochore deformation. $\bar{a} = a/r_c$, $\bar{b} = b/r_c$, where r_c is the size of the spherical solid core at $\lambda_p = 1$.

near the core tips played a dominant role. The limited polymer mass and severe deformations of subchains in these regions hindered longitudinal swelling. The dependence of $(2\bar{a},\ 2\bar{b})$ on λ_p further supports these observations. While the microgel's long axis exhibits linear growth, the short axis remains relatively constant. The anisotropy of the swollen part of the microgel in the region (iii) also decreases (Fig. 5*C*, green symbols). Due to the redistribution of polymeric mass toward region (ii), the size of the long axis reduces, compared to the value of the long axis in solution. At the same time, the size of the short axis increases, providing extra elongation of the adsorbed polymeric layer laterally in the region (ii). The interfacial aspect ratio (ρ_{int}) also scaled linearly with λ_p ($\rho_{\text{int}} \approx 0.36 \times \lambda_p$). This finding aligns with experimental results, as the overall scaling of ρ scales nearly linearly with λ_p was consistent for all three microgel states (collapsed, swollen, and at the interface), reproducing the relative slope variations observed experimentally for ρ_{TEM}, ρ_{CLSM}, and ρ_{int} (See *SI Appendix*, Fig. S18 and section 6C for further details on the comparison between experiments and simulations).

DPD simulations offer a promising avenue to elucidate interfacial deformation around core-shell microgels, particularly when comparing bare PS core particles to those surrounded by a PNIPMAM polymeric shell. This approach enables us to underline the influence of particle asphericity and shell deformability on interfacial behavior. Consistent with experimental findings, our simulations assumed a contact angle of approximately 90° for pure bare PS cores (*SI Appendix*). By quantifying particle protrusion into the air and water phases for various aspect ratios (λ_p), we found that the bare particles position themselves nearly equidistantly at the interface (*SI Appendix*, Fig. S19). Intriguingly, interfacial deformation around the bare particle exhibited minimal variation along the contact line, irrespective of (λ_p). Only at exceedingly high aspect ratios were subtle differences in contact line height discernible (Δz). These results align with theoretical predictions ($\Delta z \sim 0$ for $\alpha \sim 90°$ detailed in *SI Appendix*, Fig. S2), suggesting negligible capillary interactions for pure bare PS particles.

We subsequently investigated interfacial deformations induced by soft core-shell microgels. Initial analysis focused on microgel protrusion into the air and water phases. The heights of the anisotropic microgels for the different values of aspect ratio are shown in *SI Appendix*, Fig. S20. The height of the water–swollen part of the samples (region iii) is slightly larger than the size of the short semiaxis of the corresponding microgels in the bulk solution. The samples demonstrate a decrease in the height of the swollen part of the polymeric shell upon increasing λ_p. Due to the presence of the solid core, we observe the pronounced area of the protrusion of the microgel into the air, region (i). Microgels with more spherical shapes demonstrate greater immersion into the air phase. h_{air} has a maximum value for the spherical microgel and drops upon increasing λ_p.

The positioning of the solid core within the microgel at the interface is particularly noteworthy. Despite its hydrophobic nature, the core exhibits a greater immersion in the aqueous phase compared to the case of bare particle (Fig. 6*A* and *SI Appendix*, Fig. S19). This phenomenon can be attributed to two primary factors. First, the microgel's polymer shell tends to elongate along the interface to minimize unfavorable water–air contact, resulting in the polymeric network deformation. The position of the particle, constrained by the polymeric network, correlates with the deformation of the shell. Second, the hydrophobic PS core is partially shielded by the hydrophilic polymer shell, effectively reducing its overall hydrophobicity. Nevertheless, this behavior leads to a perturbation of the interfacial boundary that starts in the immediate vicinity of the core. Fig. 6*A* (*Top* row) provides an overview of the contact line of water near the core. To analyze local curvature, we generated averaged interface deformation images (Fig. 6*C* and *SI Appendix*, Fig. S21) for various λ_p by combining multiple snapshot frames. The deformation field is most pronounced near the solid core's periphery, with its extent influenced by the particle aspect ratio. For spherical core microgels ($\rho_c = 1$), the surface distortion is relatively symmetric but highly inhomogeneous. Despite this symmetry, interfacial wrinkles and irregularities are evident around the

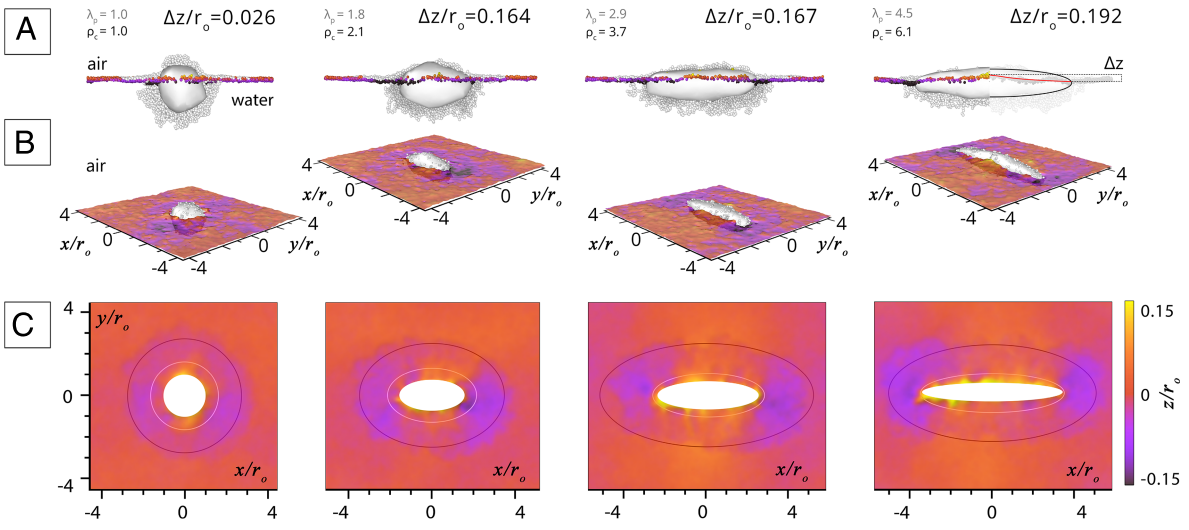

Fig. 6. Interface deformations by soft core-shell microgels as revealed by coarse-grained simulations. (*A*) Side view of microgels indicating the extent to which they are protruding into air and water. Colored beads represent the contact line of water near the solid core. The solid cores are depicted with surface meshes. Gray beads represent the shell. Δz is the maximum height difference of the contact line. r_o is the size of the spherical solid core at $\lambda_p = 1$. (*B*) 3D simulation snapshots of the solid core of the microgels (shells are not shown) with increasing aspect ratio at the water/air interface. The interface fluctuations are colored using a purple-to-orange-to-yellow gradient palette. (*C*) Averaged interface deformations overlaid with the overall dimensions of the core-shell microgels. The ellipses filled in white color schematically represent the cores. We distinguish between the immersed microgel body (green ellipse) and the highly stretched PNIPMAM shell at the interface (blue ellipse).

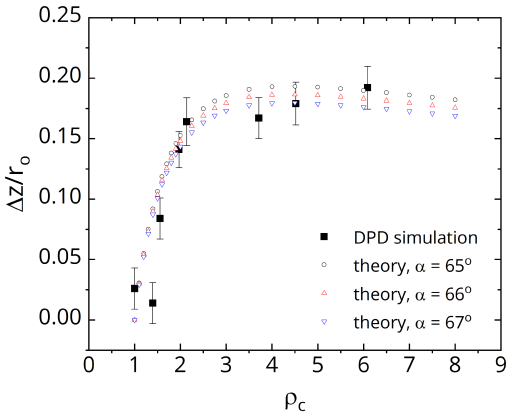

Fig. 7. The relative maximum height difference of the contact line, $\Delta\bar{z} = \Delta z/r_o$ is plotted as a function of core aspect ratio ρ_c, where r_o is the size of the spherical solid core at $\lambda_p = 1$. Hollow symbols depict theoretical calculations based on *SI Appendix*, Eqs. **S5–S8** in for contact angles of 65°, 66°, and 67° (black circles, red, and blue triangles).

core. These observations suggest that initial capillary interactions originate from contact line fluctuations. This likely induces microgel assemblies to form small clusters. In the case of the microgel with asymmetry, our findings indicate that the contact line is elevated along the microgel's short axis (high curvature region) and depressed along its long axis (low curvature region). The resulting height difference of the contact line between the short and long axes, $\Delta\bar{z}$, is presented in Fig. 7 (39). A clear correlation between $\Delta\bar{z}$ and ρ_c is observed, with $\Delta\bar{z}$ increasing as ρ_c grows, slowing down at large ρ_c values. The capillary interactions become more prominent with increasing the aspect ratio of the ellipsoidal microgels. In the case of large ρ_c, the minimization of interface distortion becomes favorable via side-to-side assembly. For the intermediate values $\rho_c \sim 2.9$, the deformation field is a combination of the first and second cases, which could explain the stability of the triangular (*Tr*) or linear aggregate. Theoretical calculations based on *SI Appendix*, Eqs. **S5–S8** yield effective contact angles of approximately 65°. The continuum model calculations were extended to a core-shell geometry with a constant contact angle at the core and a shell modeled as a lateral spacer. We find that the lateral spreading of the microgels destabilizes the side-by-side arrangement. The stability of triangular/hexagonal and side-by-side assembles as a function of the spacer length is discussed in *SI Appendix*, Section 7B.

Conclusion

This study addresses the role of shape anisotropy and softness on the capillary forces-driven assembly of ellipsoidal core-shell microgels obtained via uniaxial stretching. Supported by computer simulations, we conclude that the stretching procedure results in a significant change in the ellipsoidal microgels' deformation at the air–water interface. Unlike the original spherical core-shell microgels, the postprocessed microgels do present strong capillary interactions resulting in a transition from a *Tr* (triangular) to *SS* (side-by-side) assembly with increasing λ as is predicted for hard ellipsoids in our simulations. However, unlike hard ellipsoids, they significantly deform at the interface. Such deformation is mostly lateral resulting in much lower ρ at the interface. The transition in the assembly is observed for ρ_{int} comprised between 1.68 and 2.08. From the calculation on hard ellipsoids, it would correspond to "effective" hard ellipsoids with a contact angle between circa 40° similar to the one reported on PNIPAM gel (40) or PNIPAM grafted glass substrate (41), even if the definition of a contact angle is highly questionable for soft, deformable systems. In addition, the elasto-capillary effect needs to be taken into consideration (47).

The analysis of the particle deformation at the interface suggests that the microgel shell is highly constrained at the tip and that the lateral deformation is strongly related to the higher local curvature. Indeed, the relative deformation of the shell is more significant for the systems presenting the highest aspect ratio. As such, ellipsoidal microgels effectively cover more surfaces and significantly alter their shape at the fluid interface. This was already pointed out in former studies on core-shell ellipsoidal microgels with a silica-coated hematite core from the simulations performed on different shell configurations (33, 43). A coarse-grained model of the anisotropic microgels has been created. We evaluate how the soft polymeric shell and the anisotropic shape of the microgels influence their positioning and deformation at the interface. In particular, we confirm that during the stretching, the polymeric shell becomes strongly constrained at the tip, which explains why microgels spread relatively more laterally than longitudinally. We characterized the dimensions of different core-shell microgels in solution in their collapsed and swollen state configuration and at the air–water interface. It was shown that the in silico microgels behave in accordance with their experimental counterparts when comparing their relative aspect ratios determined under these three different conditions.

DPD simulations were evaluated to quantitatively determine the interface deformation. We conclude that deformation created by the microgels is strongly dependent on the aspect ratio of the microgel and the solid core plays a prominent role, as shown from the analysis of the contact line. Our study emphasizes the synergistic impact of colloid softness, anisotropy, and design on their interfacial deformation and capillary assembly that could contribute to the fabrication of structured 2D materials (48). It further opens horizons for applications in investigations related to uptake-release of guest functional molecules (i.e., drug delivery), and heterogeneous catalysis where chemical reactions can proceed in the microgel interior being adsorbed at a liquid interface (like oil–water).

Our study also highlights the need to connect different simulation techniques around a common theoretical framework describing elastocapillary interactions in soft permeable systems, where anisotropic microgels can serve as an ideal proxy to develop such a fundamental understanding. The developed methodology is expected to bridge the gap between classical surface minimization methods and molecular simulations for soft colloidal systems, considering that both the average contact line and its fluctuations could be evaluated. These fluctuations are indeed prominent in understanding capillary interactions in microgel systems, also resulting in quadrupolar capillary attraction between spherical microgels at the interface (49) leading in some cases to spectacular assemblies (50). Future investigations should focus on this effect and its dependence on microgel dimensions, chemical composition, and architecture. A deeper understanding of the connection between anisotropic microgel deformation and their capillary assembly should also involve a detailed experimental investigation of the interfacial deformation and the resolution of the contact line. This could be achieved by applying PSI (24), freeze-fracture shadow-casting (FreSCa) (31), or by taking advantage of recent advances in atomic force microscopy (51) or superresolution microscopy (52).

Materials and Methods

Chemicals. *N*-isopropylmethacrylamide (NIPMAM; Sigma-Aldrich), *N*,*N*′-methylenebisacrylamide (BIS; Fluka), sodium dodecyl sulfate (SDS; Fluka), methacryloxyethyl thiocarbamoyl rhodamine B (MRB-dye) and potassium peroxodisulfate (KPS initiator; Fluka) were utilized as received. The purification of styrene from BASF was done by using an Al_2O_3 column. MilliQ water was employed for the synthesis and the dispersion preparation.

Core Synthesis. Polystyrene core particles were first synthesized by emulsion polymerization and then employed as seeds for radical polymerization of the cross-linked shell (53). The experimental set up for Emulsion polymerization was conducted with one liter three-necked round bottom flask equipped with a stirrer, a reflux condenser, and a thermometer. NIPMAM (2.625 g) monomer and SDS (0.014 g) were added in 50 mL MilliQ water and dissolved under continuous magnetic stirring. Then, the purified styrene (48.3 g) was added to the mixture, degassed with nitrogen for 20 min, and then heated to 80 °C under a nitrogen atmosphere. The initiator solution was prepared by dissolving 90 mg of the KPS in 9.2 mL of MilliQ water. The degassed initiator solution was added dropwise while the mixture was stirred at 300 rpm. The reaction was carried out for 8 h under a nitrogen atmosphere. The latex dispersion was then cooled down to room temperature and filtered through glass wool to remove traces of coagulum. The latex dispersion was purified by dialysis using pure MilliQ water for three weeks (Medicell, 12,000 to 14,000 Da). As a result, the core stock dispersion with a concentration of 5.1 wt% was obtained (36).

Core-Shell Microgel Synthesis. Core-shell microgels are synthesized by the seeded emulsion polymerization using the previously synthesized stock core solution (32 g). A small amount of rhodamine (MRB) dye solution (162 mg dissolved in water) helps to covalently label the particle shell. Then, monomer NIPMAM (1.61 g), BIS crosslinker (0.1 g), and the prepared rhodamine solution were added to the core solution and 57 g of water. The mixture was degassed with nitrogen for 20 min and then heated to 80 °C. After one hour, the KPS initiator solution (50 mg dissolved in 5 mL of water) was added dropwise to the round bottom flask at a constant temperature of 80 °C under a nitrogen atmosphere. The reaction was carried out for 8 h with constant stirring at 300 rpm. Afterward, the reaction mixture was cooled down to room temperature, the core-shell latex dispersion was filtered through glass wool. Then, the purification was performed with continuous dialysis using MilliQ water for two weeks.

Postprocessing of the Core-Shell Microgels into Prolates. The anisotropic core-shell microgels were prepared using the mechanical stretching method as described in our former study (8, 37, 54). In a nutshell, the core-shell particles were embedded into PVA film. Film stripes were then clamped in a custom-made automatized uniaxial deformation set-up in a silicon oil bath maintained at 145 °C. The stripes were elongated at different draw ratios $\lambda = 1 + \Delta L/L_0$ (where ΔL is the difference in length before and after stretching, and L_0 is the initial length of the film) of 1.50, 1.75, 2.00, and 5.00. The stretched films, according to their local draw ratio λ, accessible via a grid initially sketched at the surface of the film, were then cooled down to room temperature. The cleansing procedure to recover the stretched particles is also described in our former study (37). Stretching the particles above the glass transition temperature of the polystyrene core (55) confirms that the particles deform plastically, which in turn results in the postprocessing of the initially spherical core-shell microgels into ellipsoidal core-shell microgels with different elongation.

TEM. The samples were prepared by drop-casting a 1 wt% solution on a 300 mesh carbon-coated copper grid placed on a paper filter at room temperature. The micrographs were recorded on a TEM-CM100 (Philips) operating at an acceleration voltage of 80 keV.

CLSM. CLSM measurements were performed on a Leica SP5. A temperature of 20 °C was ensured by a thermostated enclose with an accuracy of ± 0.2 °C (100× immersion objective with a numerical aperture of 1.4). The samples were contained between the glass slide and a glass coverslip separated by a 120 μm spacer (Secure Seal Imaging).

DLS. The diffusion of the particles was determined using dynamic light scattering. Dilute suspensions (concentration 0.001 wt%) were measured on an ALV setup equipped with a HeNe laser ($\lambda_0 = 633$ nm), with temperatures ranging from 20 °C to 50 °C at low scattering angles ranging from 30 to 50° with 5° step. The translational diffusion coefficient D_T was determined from a first-order cumulant analysis at the different scattering angles.

Predicting Self-Assembly of Hard Ellipsoidal Particles. The energy of smooth, hard ellipsoidal particles at interfaces is given

$$E = \gamma_{lv} S_{lv} + \gamma_{sv} S_{sv} + \gamma_{sl} S_{sl}, \quad [1]$$

where γ_{lv}, γ_{sv}, and γ_{sl} are the interface tensions and S_{lv}, S_{sv}, and S_{sl} the interface areas (17). Here, *s* indicates the solid particles, *l* the liquid phase, and *v* the vapor phase (or another liquid phase). The contact angle α is determined by force balance at the contact line and satisfies the Young–Dupré equation $\gamma_{sv} = \gamma_{lv} \cos\alpha + \gamma_{sl}$. Stable states correspond to energy minima. We use triangulated surfaces and employ the freely available program package "Surface Evolver" to predict interface shapes and corresponding, minimal total energies for various particle assemblies (56). The interface is initially set up using first-order Lagrange elements, where edges are straight lines bounding planar triangular faces; it is bounded by a wire frame. In addition to the interface shape, also the particle height above the wire frame is used as an optimization parameter. During energy minimization, the triangulation is refined, and the energy is minimized in alternating steps. In order to achieve high accuracy for the energies, second-order Lagrange elements are used for the final minimization steps. The boundaries between the stable structures of the particle assemblies are determined by the intersections of the fits through the data points describing the energy gain for single particles at interfaces to assemble into larger structures for various aspect ratios; see *SI Appendix*, Fig. S3 and the corresponding discussion in *SI Appendix*.

Fluorescence Imaging of the Interfacial Assembly. Fluorescence measurements were performed using an inverted Fluorescence Microscope (Nikon Eclipse TE300) at 20 °C that was connected to a Blackfly S BFS-U3-04S2M camera. A Nikon Plan Fluor Oil NA 0.5 to 1.3 objective with a magnification of 100X was used. A thermostated enclosure from Okolab was utilized as a temperature controller, which leads to a temperature accuracy of less than 0.1 °C. Fluorescence imaging was performed using a Nikon Intensilight light source and fluorescence filters adapted to rhodamine B. Imaging of the particles at interfaces was conducted by using magnetically closed cells, details in *SI Appendix*, Fig. S5).

Image Processing of the Interfacial Assembly. The fluorescence micrographs were processed using a Matlab routine based on our previous work (57). Since the raw images had uneven brightness, a binary mask was created to improve particle localization. The mask was calculated by multilevel thresholding and size filtering of the bright objects, which was possible due to the low polydispersity of the core-shell microgels. A linear interpolated grayscale image (factor 2.5) and the binary mask were handed to the Matlab function *regionprops* determining the weighted center, the dimensions, and the orientation of the microgels. A Delaunay triangulation was performed to find the interparticle connections. The resulting connectivity list and the orientation of the particles were used to characterize their triangular, squared, or side-to-side ordering.

Atomic Force Microscopy (AFM). The sample was prepared by the dip-coating technique on a glass coverslip with a size of 24 × 50 mm using a custom-designed dipcoater described in more detail in *SI Appendix*. The configuration of the soft microgels at the air–water interface was investigated in the dried state in tapping mode using OTESPA tips with a resonance frequency of 300 kHz, a nominal spring constant of 26 N m^{-1} of the cantilever, and a nominal tip radius of <7 nm (NanoAndMore GmbH, Germany). The distribution of PNIPMAM shell was investigated in water in the Peak Force QNM mode. The measurements were performed at 27 °C using MSNL-10-E tip (Bruker) with a nominal resonance frequency of 38 kHz in air and a nominal spring constant of 0.1 N/m (tip radius: 2 nm, semiangle of the tip: 23°, assumed sample Poisson's ratio: 0.3). The obtained data were analyzed by original NanoScope Software and custom-made MATLAB script based on ref. 58, more information can be found in *SI Appendix*.

Simulation. To extend knowledge of the behavior of the anisotropic core-shell microgels in bulk and at the air–water interface, DPD simulations have been performed. Based on the deformation of the spherical core-shell particles in the cylindrical confinement, we have developed a model and algorithm for forming ellipsoidal core-shell microgels of different aspect ratios.

First, NIPMAM-based microgels with the spherical PS core have been obtained. The microgels were created in such a way as to follow the experimental values of core-to-shell ratio $2a/2a_c$ in bulk, both in dry and swollen states (for details, we refer to *SI Appendix*, section 4A and B). Afterward, based on the suitable spherical sample, a series of ellipsoidal microgels of different aspect ratios were produced.

The key idea of the experimental method behind the formation of ellipsoidal microgels is based on the change in the mechanical properties of the PS core below and above the glass transition temperature (T_g) (54). The PS core represents the complex kinetically arrested system (59–61). Rapid heat of the PS above T_g followed by a stretching and then rapid cooling below T_g ensure plastic deformation of the core and "freezes-in" the new particle shape. In the simulations, we create a model of the PS core and set the parameters in such a way to ensure the plastic deformation mechanism for the coarse-grained core, preserving its volume when changing the shape. Moreover, the model considers the presence of junction points between the NIPMAM shell and PS chains and provides data about its redistribution under the constraints (for details, we refer to *SI Appendix*, section 4C).

To get the ellipsoidal microgels in simulations, we used cylindrical pores of different diameters to provoke the uniaxial stretching process for a different draw ratio. Parameter $\lambda_p = (R_0/R)^2$ is used to denote the sample, where R is the pore size, while R_0 is the size of the spherical microgel in bulk.

We consider an originally spherical particle of radius R_0. When confined in the cylindrical pores of radius R, the particle adopts an ellipsoidal shape defined by the semi-long and short axes a and b, respectively. For an isochore transformation, $a \cdot b^2 = R_0^3$. When $R < R_0$, as $b = R$ the particle elongates and $a = \lambda_p \cdot R_0$. In analogy to the stretching experiments in the simulation under cylindrical pore confinement, from the volume conservation, $\lambda_p \cdot R_0 \cdot R^2 = R_0^3$ and therefore $\lambda_p = (R_0/R)^2$. A similar scaling as in the experiments is thus expected when the particle deformation is reported as a function of λ_p. All computations were performed on high-performance computing resources of the Lomonosov Moscow University (62).

Data, Materials, and Software Availability. Raw dynamic light scattering measurements (.txt), raw and processed fluorescence micrographs (.tif), the data relevant for Fig. 2 (*.gp gnuplot, *.dat, and some python script *.py), the data for Figs. 4, 5, and 7 (*.txt), as well as some raw AFM measurements (*.spm data) and the data from *SI Appendix*, Fig. S9 as Matlab figure have been deposited in RADAR4Chem (DOI: 10.22000/dh0vt37bfcfnyf62) (39).

ACKNOWLEDGMENTS. We gratefully acknowledge financial support from the Deutsche Forschungsgemeinschaft within the Sonderforschungsbereich 985 "Functional Microgels and Microgel Systems." We thank Patrick Pfleiderer and Jan Vermant for the postprocessing of the core-shell microgels into ellipsoids, Simon Schog for the code to analyze the Atomic force microscopy force measurements, and Olli-Ville Laukanen for the help with test interface experiments. The computer simulations were carried out under financial support from the Russian Science Foundation, project 21-73-30013, using the equipment of the shared research facilities of high-performance computing computing resources at Lomonosov Moscow State University (Supercomputer Lomonosov-2).

Author affiliations: [a]Institute of Physical Chemistry, Rheinisch-Westfälische Technische Hochschule Aachen University, Aachen 52074, Germany; [b]Deutsches Wollforschungsinstitut Leibniz-Institute for Interactive Materials, Aachen 52074, Germany; [c]Physics Department, Lomonosov Moscow State University, Moscow 119991, Russian Federation; and [d]Theoretical Physics of Living Matter, Institute of Biological Information Processing and Institute for Advanced Simulation, Forschungszentrum Jülich, Jülich 52428, Germany

1. F. A. Plamper, W. Richtering, Functional microgels and microgel systems. *Acc. Chem. Res.* **50**, 131–140 (2017).
2. M. Karg *et al*., Nanogels and microgels: From model colloids to applications, recent developments, and future trends. *Langmuir* **35**, 6231–6255 (2019).
3. C. D. Jones, L. A. Lyon, Shell-restricted swelling and core compression in poly(*N*-isopropylacrylamide) core- shell microgels. *Macromolecules* **36**, 1988–1993 (2003).
4. G. M. Conley, P. Aebischer, S. Nöjd, P. Schurtenberger, F. Scheffold, Jamming and overpacking fuzzy microgels: Deformation, interpenetration, and compression. *Sci. Adv.* **3**, e1700969 (2017).
5. A. Scotti *et al*., Experimental determination of the bulk moduli of hollow nanogels. *Soft Matter* **18**, 5750–5758 (2022).
6. P. S. Mohanty, D. Paloli, J. J. Crassous, E. Zaccarelli, P. Schurtenberger, Effective interactions between soft-repulsive colloids: Experiments, theory, and simulations. *J. Chem. Phys.* **140**, 094901 (2014).
7. S. Wiese, A. C. Spiess, W. Richtering, Microgel-stabilized smart emulsions for biocatalysis. *Angew. Chem.* **125**, 604–607 (2013).
8. B. Madivala, S. Vandebril, J. Fransaer, J. Vermant, Exploiting particle shape in solid stabilized emulsions. *Soft Matter* **5**, 1717–1727 (2009).
9. L. A. Lyon, A. Fernandez-Nieves, The polymer/colloid duality of microgel suspensions. *Annu. Rev. Phys. Chem.* **63**, 25–43 (2012).
10. N. Ballard, A. D. Law, S. A. Bon, Colloidal particles at fluid interfaces: Behaviour of isolated particles. *Soft Matter* **15**, 1186–1199 (2019).
11. S. Dasgupta, T. Auth, G. Gompper, Nano-and microparticles at fluid and biological interfaces. *J. Phys. Condens. Matter* **29**, 373003 (2017).
12. L. Botto, E. P. Lewandowski, M. Cavallaro, K. J. Stebe, Capillary interactions between anisotropic particles. *Soft Matter* **8**, 9957–9971 (2012).
13. P. A. Kralchevsky, K. Nagayama, Capillary interactions between particles bound to interfaces, liquid films and biomembranes. *Adv. Colloid Interface Sci.* **85**, 145–192 (2000).
14. D. Stamou, C. Duschl, D. Johannsmann, Long-range attraction between colloidal spheres at the air-water interface: The consequence of an irregular meniscus. *Phys. Rev. E* **62**, 5263 (2000).
15. D. Vella, L. Mahadevan, The "cheerios effect". *Am. J. Phys.* **73**, 817–825 (2005).
16. J. C. Loudet, A. M. Alsayed, J. Zhang, A. G. Yodh, Capillary interactions between anisotropic colloidal particles. *Phys. Rev. Lett.* **94**, 018301 (2005).
17. S. Dasgupta, M. Katava, M. Faraj, T. Auth, G. Gompper, Capillary assembly of microscale ellipsoidal, cuboidal, and spherical particles at interfaces. *Langmuir* **30**, 11873–11882 (2014).
18. E. P. Lewandowski *et al*., Orientation and self-assembly of cylindrical particles by anisotropic capillary interactions. *Langmuir* **26**, 15142–15154 (2010).
19. G. Soligno, M. Dijkstra, R. van Roij, Self-assembly of cubes into 2D hexagonal and honeycomb lattices by hexapolar capillary interactions. *Phys. Rev. Lett.* **116**, 258001 (2016).
20. D. Ershov, J. Sprakel, J. Appel, M. A. Cohen Stuart, J. van der Gucht, Capillarity-induced ordering of spherical colloids on an interface with anisotropic curvature. *Proc. Natl. Acad. Sci. U.S.A.* **110**, 9220–9224 (2013).
21. M. Cavallaro Jr., L. Botto, E. P. Lewandowski, M. Wang, K. J. Stebe, Curvature-driven capillary migration and assembly of rod-like particles. *Proc. Natl. Acad. Sci. U.S.A.* **108**, 20923–20928 (2011).
22. B. Madivala, J. Fransaer, J. Vermant, Self-assembly and rheology of ellipsoidal particles at interfaces. *Langmuir* **25**, 2718–2728 (2009).
23. M. Oettel, S. Dietrich, Colloidal interactions at fluid interfaces. *Langmuir* **24**, 1425–1441 (2008).
24. J. C. Loudet, A. G. Yodh, B. Pouligny, Wetting and contact lines of micrometer-sized ellipsoids. *Phys. Rev. Lett.* **97**, 018304 (2006).
25. H. Lehle, E. Noruzifar, M. Oettel, Ellipsoidal particles at fluid interfaces. *Eur. Phys. J. E* **26**, 151–160 (2008).
26. J. C. Loudet, B. Pouligny, How do mosquito eggs self-assemble on the water surface? *Eur. Phys. J. E* **34**, 1–17 (2011).
27. C. C. Ho, A. Keller, J. A. Odell, R. H. Ottewill, Preparation of monodisperse ellipsoidal polystyrene particles. *Colloid Polym. Sci.* **271**, 469–479 (1993).
28. K. Geisel, L. Isa, W. Richtering, Unraveling the 3D localization and deformation of responsive microgels at oil/water interfaces: A step forward in understanding soft emulsion stabilizers. *Langmuir* **28**, 15770–15776 (2012).
29. A. M. Mihut, A. P. Dabkowska, J. J. Crassous, P. Schurtenberger, T. Nylander, Tunable adsorption of soft colloids on model biomembranes. *ACS Nano* **7**, 10752–10763 (2013).
30. F. Pinaud *et al*., Adsorption of microgels at an oil-water interface: Correlation between packing and 2D elasticity. *Soft Matter* **10**, 6963–6974 (2014).
31. F. Camerin *et al*., Microgels adsorbed at liquid-liquid interfaces: A joint numerical and experimental study. *ACS Nano* **13**, 4548–4559 (2019).
32. S. Bochenek *et al*., In-situ study of the impact of temperature and architecture on the interfacial structure of microgels. *Nat. Commun.* **13**, 1–12 (2022).
33. A. C. Nickel *et al*., Anisotropic microgels show their soft side. *Langmuir* **38**, 5063–5080 (2021).
34. A. C. Nickel *et al*., Anisotropic hollow microgels that can adapt their size, shape, and softness. *Nano Lett.* **19**, 8161–8170 (2019).
35. K. Honda *et al*., Hydrogel microellipsoids that form robust string-like assemblies at the air/water interface. *Angew. Chem. Int. Ed.* **58**, 7294–7298 (2019).
36. J. J. Crassous *et al*., Preparation and characterization of ellipsoidal-shaped thermosensitive microgel colloids with tailored aspect ratios. *Soft Matter* **8**, 3538–3548 (2012).
37. J. J. Crassous *et al*., Field-induced assembly of colloidal ellipsoids into well-defined microtubules. *Nat. Commun.* **5**, 1–7 (2014).
38. D. Benke *et al*., Prolate spheroidal polystyrene nanoparticles: Matrix assisted synthesis, interface properties, and scattering analysis. *Soft Matter* **19**, 9006–9016 (2023).
39. J. J. Crassous, Dataset belonging to the Publication: "Capillary Driven Self-Assembly of Soft Ellipsoidal Microgels at the Air/Water Interface." RADAR4Chem. https://doi.org/10.22000/dh0vt37bfcfnyf62. Deposited 24 November 2024.
40. J. Zhang, R. Pelton, Y. Deng, Temperature-dependent contact angles of water on poly(*N*-isopropylacrylamide) gels. *Langmuir* **11**, 2301 (1995).

41. Y. G. Takei *et al*., Dynamic contact angle measurement of temperature-responsive surface properties for poly(*N*-isopropylacrylamide) grafted surfaces. *Macromolecules* **27**, 6163–6166 (1994).
42. D. Y. Kwok *et al*., Low-rate dynamic contact angles on polystyrene and the determination of solid surface tensions. *Polym. Eng. Sci.* **38**, 1675–1684 (1998).
43. A. C. Nickel, A. A. Rudov, I. I. Potemkin, J. J. Crassous, W. Richtering, Interfacial assembly of anisotropic core-shell and hollow microgels. *Langmuir* **38**, 4351–4363 (2022).
44. J. Hubbard, J. Douglas, Hydrodynamic friction and the capacitance of arbitrarily shaped objects. *Phys. Rev. E* **47**, R2983–R2986 (1993).
45. J. Douglas, H. X. Zhou, J. Hubbard, Hydrodynamic friction and the capacitance of arbitrarily shaped objects. *Phys. Rev. E* **49**, 5319–5337 (1994).
46. L. Hoppe Alvarez *et al*., Controlling microgel deformation via deposition method and surface functionalization of solid supports. *Phys. Chem. Chem. Phys.* **23**, 4927–4934 (2021).
47. R. W. Style, L. Isa, E. R. Dufresne, Adsorption of soft particles at fluid interfaces. *Soft Matter* **11**, 7412–7419 (2015).
48. B. M. Rey *et al*., Fully tunable silicon nanowire arrays fabricated by soft nanoparticle templating. *Nano Lett.* **16**, 157–163, PMID: 26672801 (2016).
49. M. A. Fernandez-Rodriguez, M. N. Antonopoulou, L. Isa, Near-zero surface pressure assembly of rectangular lattices of microgels at fluid interfaces for colloidal lithography. *Soft Matter* **17**, 335–340 (2021).
50. F. Grillo, M. A. Fernandez-Rodriguez, M. N. Antonopoulou, D. Gerber, L. Isa, Self-templating assembly of soft microparticles into complex tessellations. *Nature* **582**, 219–224 (2020).
51. J. Vialetto, S. N. Ramakrishna, L. Isa, In situ imaging of the three-dimensional shape of soft responsive particles at fluid interfaces by atomic force microscopy. *Sci. Adv.* **8**, eabq2019 (2022).
52. O. Nevskyi, D. Wöll, 3D super-resolution fluorescence imaging of microgels. *Annu. Rev. Phys. Chem.* **74**, 391–414 (2023).
53. N. Dingenouts *et al*., Analysis of thermosensitive core-shell colloids by small-angle neutron scattering including contrast variation. *Phys. Chem. Chem. Phys.* **3**, 1169–1174 (2001).
54. C. Ho, A. Keller, J. Odell, R. Ottewill, Preparation of monodisperse ellipsoidal polystyrene particles. *Colloid Polym. Sci.* **271**, 469–479 (1993).
55. E. Grulke 3rd, *In Polymer Handbook* (brandrup j, immergut eh, 1989), ed. 3, vol. 6.
56. K. A. Brakke, The surface evolver. *Exp. Math.* **1**, 141–165 (1992).
57. S. Bochenek, A. Scotti, W. Richtering, Temperature-sensitive soft microgels at interfaces: Air-water versus oil-water. *Soft Matter* **17**, 976–988 (2021).
58. M. F. Schulte *et al*., Stiffness tomography of ultra-soft nanogels by atomic force microscopy. *Angew. Chem. Int. Ed.* **60**, 2280–2287 (2021).
59. G. Zhang *et al*., Hierarchical modelling of polystyrene melts: From soft blobs to atomistic resolution. *Soft Matter* **15**, 289–302 (2019).
60. J. Wang, P. J. in 't Veld, M. O. Robbins, T. Ge, Effects of coarse-graining on molecular simulation of craze formation in polymer glass. *Macromolecules* **55**, 1267–1278 (2022).
61. H. P. Hsu, K. Kremer, A coarse-grained polymer model for studying the glass transition. *J. Chem. Phys.* **150**, 091101 (2019).
62. V. V. Voevodin *et al*., Supercomputer lomonosov-2: Large scale, deep monitoring and fine analytics for the user community. *Supercomput. Front. Innov.* **6**, 4–11 (2019).